ADVANCED ELECTRONIC MATERIALS Open Access
www.advelectronicmat.de

Development Aramid Nanofiber- and Pentaerythritol-Grafted Graphene Nanoplate-Based High-Performance Thermally Conductive Composites

*Wondu Lee, Wonyoung Yang, and Jooheon Kim**

A novel filler surface treatment is employed to produce thermally conductive composites using an aramid nanofiber (ANF) and pentaerythritol (PER) grafted onto the surface of graphite nanoplates (GnP). The resulting composite exhibits exceptional properties, including a high through-plane thermal conductivity of 4 W mK^{-1}, a high tensile strength of 163.58 MPa, and an improved flame retardancy. When the composite is applicated in central processing unit (CPU), the efficient thermal management performance is achieved with a decreased operating temperature of 12 °C. The ANF/GnP–PERANF composites are promising for enhancing thermal management in electric devices. The manufactured ANF composites will open new avenues for advancing the development of next-generation thermal management systems.

1. Introduction

The advent of next-generation technology has given rise to lightweight, miniaturized, and multifunctional devices that are now a reality. These devices include micro light-emitting diodes (μLEDs), flexible printed circuit boards (FPCBs), and automobiles.[1,2,3] However, a major challenge in these highly integrated electric devices is the construction of efficient thermal management systems.[4,5] Particularly, dealing with the excessive heat buildup in electric vehicles poses a significant challenge for the industry. To address this issue and achieve effective thermal management, thermal interface materials (TIMs) such as polymer composites are employed.[6,7] Typically, thermally conductive composites are created by combining polymer materials like epoxy,[8] polyvinyl alcohol,[9] polyimide,[10] cellulose nanofibers (CNF),[11] and aramid nanofiber (ANF).[12] While polymers offer advantages such as processability, affordability, and lightweight, their intrinsic thermal conductivity is below 0.5 W mK^{-1}.[13,14] To enhance the thermal conductivity of polymers, various thermally conductive fillers such as boron nitride,[15] aluminum nitride,[16] graphene,[17] and carbon nanotube[18] are incorporated into the polymer matrix. The lightweight nature, high specific strength, and impressive high-temperature resistance of ANF composites have garnered significant attention. Additionally, their capacity to retain exceptional mechanical and electrical insulating properties in scenarios encompassing varying temperature and humidity levels further enhances their appeal.[19] In a study by Han et al, they crafted thermally conductive composite films that outperformed in electromagnetic interference shielding and joule heating. This feat was achieved by employing BN nanosheets and silver nanowires as hybrid fillers. Notably, these composites exhibited remarkable attributes, including a notable in-plane thermal conductivity of 8.12 W mK^{-1}, an outstanding tensile strength of 122.9 MPa, and an impressive electromagnetic interference shielding effectiveness of 70 dB.[20] However, achieving high-performance composites requires more than just a simple dispersion of fillers within the polymer matrix. Researchers have explored the functionalization of fillers to improve their properties within the polymer matrix by grafting functional groups onto their surfaces.[21,22] Due to the ease of functionalization of carbon-based fillers, various studies have been conducted to treat these fillers.[23,24,25] A particularly effective approach involves functionalizing fillers to improve their interaction at interfaces and to control their alignment within the polymer matrix.[26,27] Ruan et al. accomplished the alignment of graphene fluoride within a PI matrix through liquid crystalline modification, resulting in composites with a substantial 446.8% enhancement in thermal conductivity, reaching 4.21 W mK^{-1}.[28] However, despite the multitude of research findings, the

W. Lee, W. Yang, J. Kim
School of Chemical Engineering and Materials Science
Chung-Ang University
Seoul 156-756, Republic of Korea
E-mail: jooheonkim@cau.ac.kr
J. Kim
Department of Advanced Materials Engineering
Chung-Ang University
Anseong-si, Gyeonggi-do 17546, Republic of Korea
J. Kim
Graduate School of Intelligence Energy and Industry
Chung-Ang University
Seoul 06974, Republic of Korea

The ORCID identification number(s) for the author(s) of this article can be found under https://doi.org/10.1002/aelm.202300455

© 2023 The Authors. Advanced Electronic Materials published by Wiley-VCH GmbH. This is an open access article under the terms of the Creative Commons Attribution License, which permits use, distribution and reproduction in any medium, provided the original work is properly cited.

DOI: 10.1002/aelm.202300455

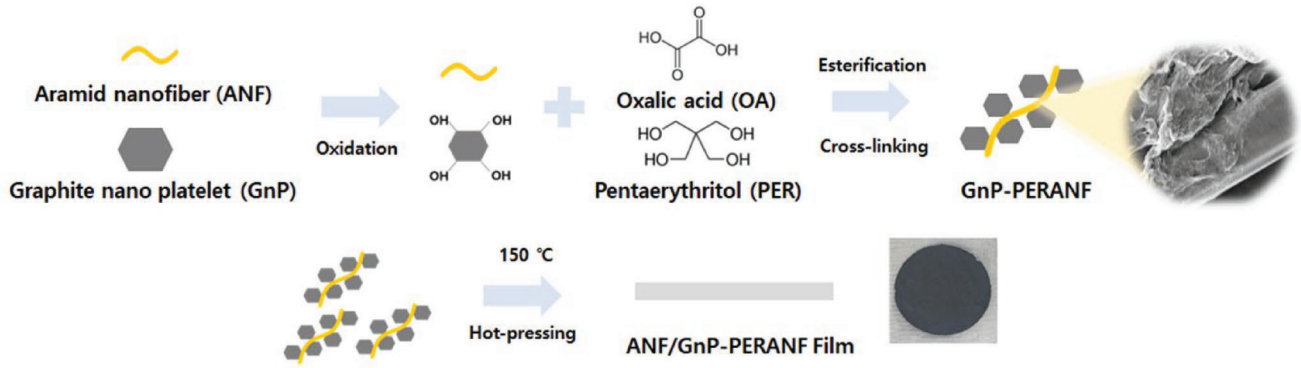


Figure 1. Schematic illustration of the ANF composites.

incorporation of high filler concentrations can potentially compromise the intrinsic properties of polymers. Thus, there is a need for further investigation to devise an approach that optimizes filler characteristics while concurrently minimizing any degradation of the polymer matrix.

In this study, we introduce an innovative approach for treating aramid nanofiber (ANF) and pentaerythritol (PER)-grafted graphite nanoplates (GnP). The treatment involves esterification of ANF and PER on the surface of oxidized GnP. The resulting GnP–PERANF system is then dispersed within ANF and undergoes hot-pressing to produce ANF composites with outstanding performance characteristics. The grafted ANF, along with the hydrophilic functional groups present on the GnP surface, promote hydrogen bonding between the fillers and the ANF matrix. This hydrogen bonding plays a crucial role in significantly enhancing the thermal conductivity, mechanical properties, and flame retardancy of the composites. By employing this fabrication method and creating the synthesized novel high-performance composite, we anticipate an accelerated advancement in the development of advanced TIM (Thermal Interface Material) composites.

2. Results and Discussion

The preparation of thermally conductive polymer composites involved a series of filler functionalization and fabrication methods, as depicted in **Figure 1**. The GnP surface underwent oxidation and esterification processes to facilitate the chemical reaction of ANFs and PER. Through this functionalization approach, the compatibility between the fillers and the matrix was enhanced, leading to improved mechanical properties in the ANF composites.

The treatment process was analyzed using Fourier transform infrared (FTIR) spectroscopy to observe the alterations in chemical bonds. **Figure 2**a showcases the FTIR spectra of raw GnP, PER, and GnP–PER. Upon grafting PER, the GnP–PER spectrum displays a new peak at 3320 cm^{-1} with a broad intensity range, which corresponds to the stretching vibrations of the O—H groups.[29] An additional peak arises at 1215 cm^{-1}, which can be attributed to the breathing vibrations of O—C—O.[30] In Figure 2b, additional peaks are evident in the FTIR spectra of GnP–PERANF following the reaction with PER and ANFs. These peaks are attributed to the vibrations of the —NH groups in the ANFs, prominently observed at 3250 cm^{-1}.[31] During the

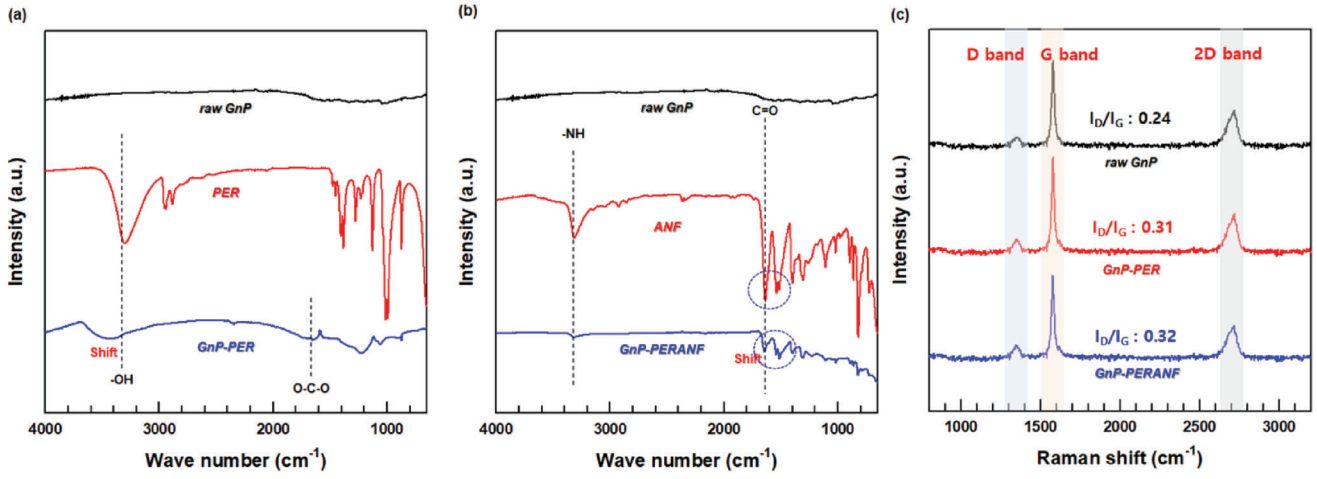


Figure 2. a,b) FT-IR spectra, c) Raman shift according to esterification.

© 2023 The Authors. Advanced Electronic Materials published by Wiley-VCH GmbH

2199160x, 2023, 12, Downloaded from https://onlinelibrary.wiley.com/doi/10.1002/aelm.202300455 by Chung-Ang University, Wiley Online Library on [26/03/2024]. See the Terms and Conditions (https://onlinelibrary.wiley.com/terms-and-conditions) on Wiley Online Library for rules of use; OA articles are governed by the applicable Creative Commons License

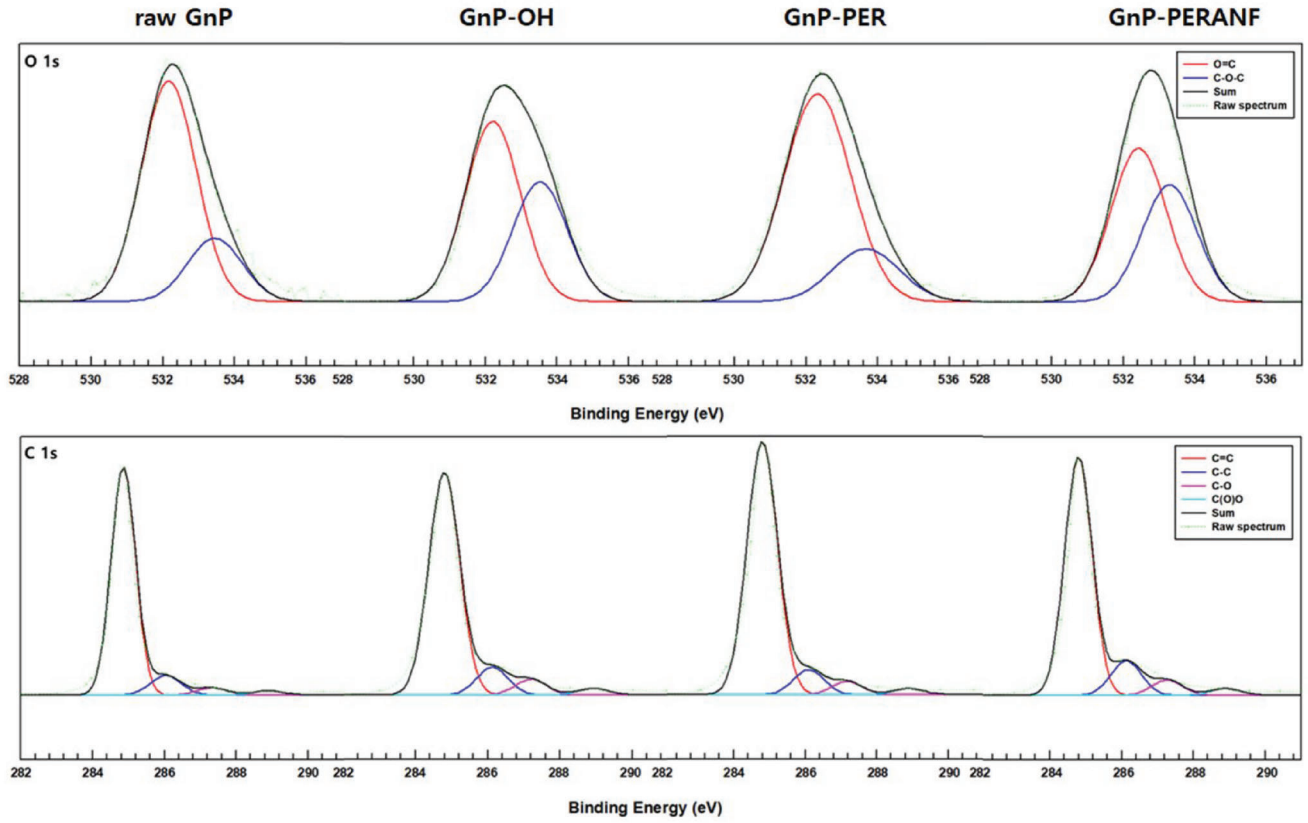


Figure 3. XPS deconvolution of raw GnP, GnP–OH, GnP–PER, and GnP–PERANF.

esterification process, oxalic acid (OA) participates, leading to concurrent hydrolysis and esterification with hydroxyl groups.[32,33] This creates an acidic catalytic environment, facilitating the bridging of hydroxyl groups on GnP–PER and ketone groups on ANF in a chemical manner. This is supported by a noticeable shift in the C═O peak, shifting from 1611 cm^{-1} in ANF to 1628 cm^{-1} in the carbonyl vibrations of esters in GnP–PERANF.[34] The FTIR observations provide strong evidence for the successful introduction of ANFs onto the GnP surface through esterification.

In order to conduct a comprehensive analysis, a range of additional techniques were employed, including Raman spectroscopy and X-ray photoelectron spectroscopy (XPS). Notably, Figure 2c presents the Raman spectrum of GnP, showcasing three distinct features: the G band, D band, and 2D band. The D band peak at 1349 cm^{-1} corresponds to the vibrations of sp3-hybridized carbon and surface defects present on GnP. Conversely, the G band peak at 1579 cm^{-1} represents the vibrations of sp2-bonded carbon atoms, while the 2D band peak at 2718 cm^{-1} arises from double-resonant Raman scattering, signifying a second-order D band.[35] The I_D/I_G ratio, which is the ratio of the D band intensity to the G band intensity, serves as a measure of disorder in carbon materials.[36] Upon the treatment of PER and PERANF, the Raman spectra of the GnP, GnP–PER, and GnP–PERANF samples reveal an increase in the I_D/I_G ratio. Specifically, the values progress from 0.24 to 0.31 and 0.32. This observed elevation in the I_D/I_G ratio indicates a rise in the number of surface defects present in GnP–PER and GnP–PERANF, attributable to the introduction of oxygen functional groups through the esterification process.

By utilizing X-ray photoelectron spectroscopy (XPS) deconvolution analysis, a comprehensive understanding of the changes in functional groups was obtained, as illustrated in **Figure 3** and **Table 1**. An intriguing finding emerged when examining the ratio of hydroxyl/ester group (C—OH/C—O—C, 533.3 eV)[37,38] to carbonyl group (O═C, 532.1 eV)[39,40] following the oxidation of raw GnP. The ratio displayed an increase, but it notably decreased after the PER treatment due to the incorporation of the C═O group during esterification. This implies that as the reaction progressed, the overall oxygen content declined while the carbon content increased. XPS data confirmed a substantial reduction in the total oxygen content, dropping from 19.68 (GnP–OH) to 6.69 (GnP–PER). However, the ratio of C═O in GnP–PER (78.71) surpassed that of GnP–OH (60.01) owing to the formation of new ester bonds during the reaction. Moreover, the ratio of C—OH/C—O—C to C═O and the total oxygen content in GnP–PERANF experienced a decrease compared to GnP–OH and GnP–PER following the reaction of PER and ANF. This observation aligns with the formation of fresh ester bonds. A similar trend was observed in the C 1s deconvolution, where the ratio of the ester group (C(O)O, 288.9 eV)[41] exhibited an increase subsequent to the oxidation of raw GnP and the esterification of ANF. These findings provide robust and compelling evidence that

© 2023 The Authors. Advanced Electronic Materials published by Wiley-VCH GmbH

2199160x, 2023, 12, Downloaded from https://onlinelibrary.wiley.com/doi/10.1002/aelm.202300455 by Chung-Ang University, Wiley Online Library on [26/03/2024]. See the Terms and Conditions (https://onlinelibrary.wiley.com/terms-and-conditions) on Wiley Online Library for rules of use; OA articles are governed by the applicable Creative Commons License

Table 1. XPS deconvolution of raw GnP, GnP–OH, GnP–PER, and GnP–PERANF.

Spectrum/Groups		raw GnP		GnP–OH		GnP–PER		GnP–PERANF	
		Ratio	Total content [%]	Ratio	Total content [%]	Ratio	Total content [%]	Ratio	Total content [%]
O 1s	O=C	75.36	1.93	60.01	19.68	78.71	6.69	58.09	11.28
	C—OH/ C—O—C	24.64		39.99		21.29		41.91	
C 1s	C=C	85.16	98.07	81.58	80.32	85.16	93.31	78.99	88.72
	C—C	8.73		10.34		8.37		12.73	
	C—O	4.06		5.84		4.43		5.84	
	C(O)O	2.05		2.24		2.04		2.44	

supports the successful introduction of ANF onto the GnP surface through the process of esterification.

Field-emission scanning electron microscopy (FESEM) was employed to investigate the morphology of the fillers, and the corresponding images are presented in **Figure 4**. Figure 4a,b showcases the fibrous nature of the ANFs and the platelet structure of GnP, respectively. Notably, the structure of GnP remains intact even after PERANF treatment, as evident in Figure 4c,d. Upon closer examination of the magnified image of the GnP surface, the successful treatment of ANFs onto the GnP surface is clearly observed.

In order to create composites with excellent performance, the GnP–PERANF prepared earlier was dispersed within an ANF matrix. The results of the cross-sectional FESEM analysis of these composites are depicted in **Figure 5**. Figure 5a exhibits the homogeneous phase of the neat ANFs. When raw GnP was incorporated as a filler, it was randomly dispersed, resulting in numerous defects in the ANF/GnP composite, as shown in Figure 5b. On the other hand, in the ANF/GnP–PERANF composite (Figure 5c), the ANFs within the matrix and on the filler surfaces intertwine to create a continuous network of fillers. This network enables efficient pathways for heat transfer in the through-plane direction and contributes to the isotropic properties of the composites. To increase the density and achieve a higher filler loading, the ANF/GnP–PERANF composite underwent a hot-pressing process, which reduced the presence of voids and facilitated the formation of a high-density, efficient heat-transfer pathway within the composites.

The specific heat capacity, density, and through-plane thermal diffusivity of the composites were measured at different filler loadings as well as based on the manufacturing method of the composites, and their thermal conductivity was calculated (see **Figure 6**a). As expected, the thermal conductivity of the ANF/GnP–PERANF composite is 4 W mK^{-1}, which is the highest recorded value at 1236% higher than that of the neat ANFs. This high conductivity can be attributed to the synergistic effect of the efficient heat-transfer paths formed by the fillers along through-plane direction and high density achieved by hot-pressing.

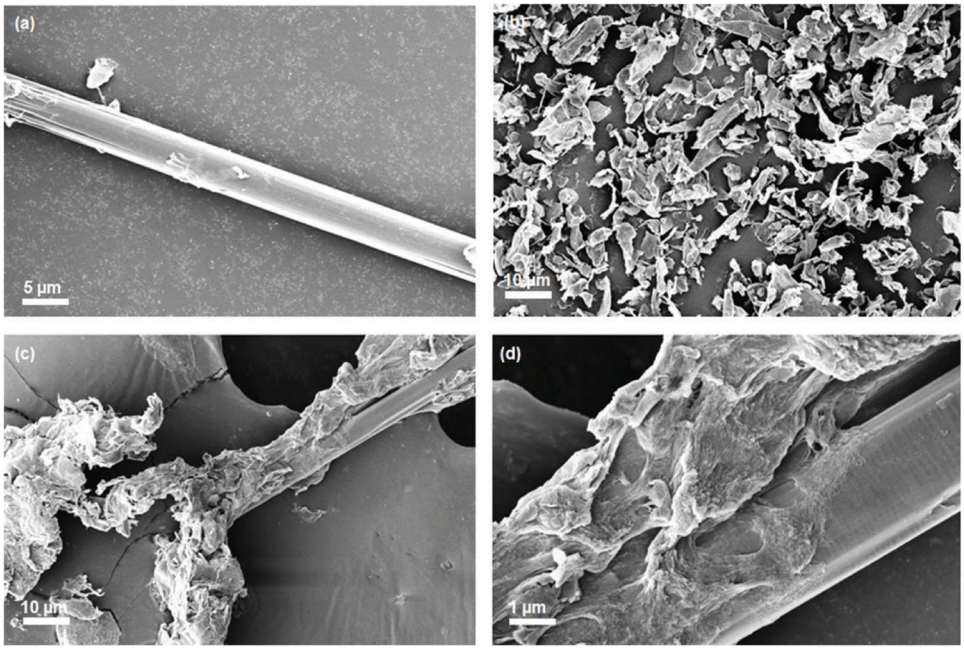


Figure 4. Morphologies of fillers: a) ANF, b) raw GnP, c,d) surface of GnP–PERANF.

© 2023 The Authors. Advanced Electronic Materials published by Wiley-VCH GmbH

2199160x, 2023, 12, Downloaded from https://onlinelibrary.wiley.com/doi/10.1002/aelm.202300455 by Chung-Ang University, Wiley Online Library on [26/03/2024]. See the Terms and Conditions (https://onlinelibrary.wiley.com/terms-and-conditions) on Wiley Online Library for rules of use; OA articles are governed by the applicable Creative Commons License

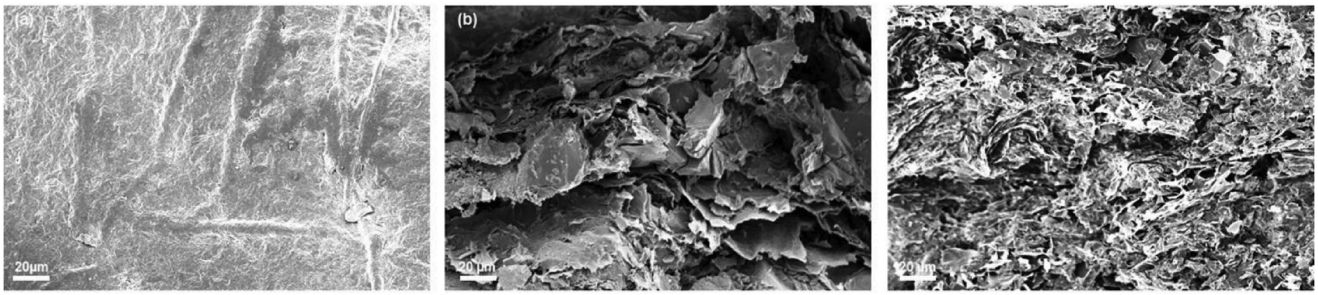


Figure 5. a) Top view of neat ANF film. Cross-sectional images of b) ANF/raw GnP and c) ANF/GnP–PERANF composites.

Additionally, a theoretical model was used to predict the thermal conductivity of the composites in order to determine the increase in the conductivity. Further, the Agari–Uno model was employed to evaluate the effect of fillers with different morphologies on the thermal conductivity of the composites with a filler concentration above the percolation threshold (the details are presented below).

For fundamentally more accurate predictions, we obtained an excellent matching for the thermal conductivities using a certain probability factor, *P*, which considers the percolated conductive path of the fillers in the composite. The Agari–Uno model is modified from the Maxwell model by considering a certain probability, *P*, which indicates the effect of fillers forming a thermally conductive network within a polymer matrix. According to this theory, the thermal conductivity can be expressed by the following equation:

$$k_c = k_m \frac{k_p + 2k_m + 2(1-P)(k_p - k_m)}{k_p + 2k_m - (1-P)(k_p - k_m)} + V_f P c^2 k_p \quad (1)$$

where c^2 is the cross-sectional area of the thermal conducting path, k_c is the thermal conductivity of a composite, k_m is the thermal conductivity of a matrix, k_p is the thermal conductivity of

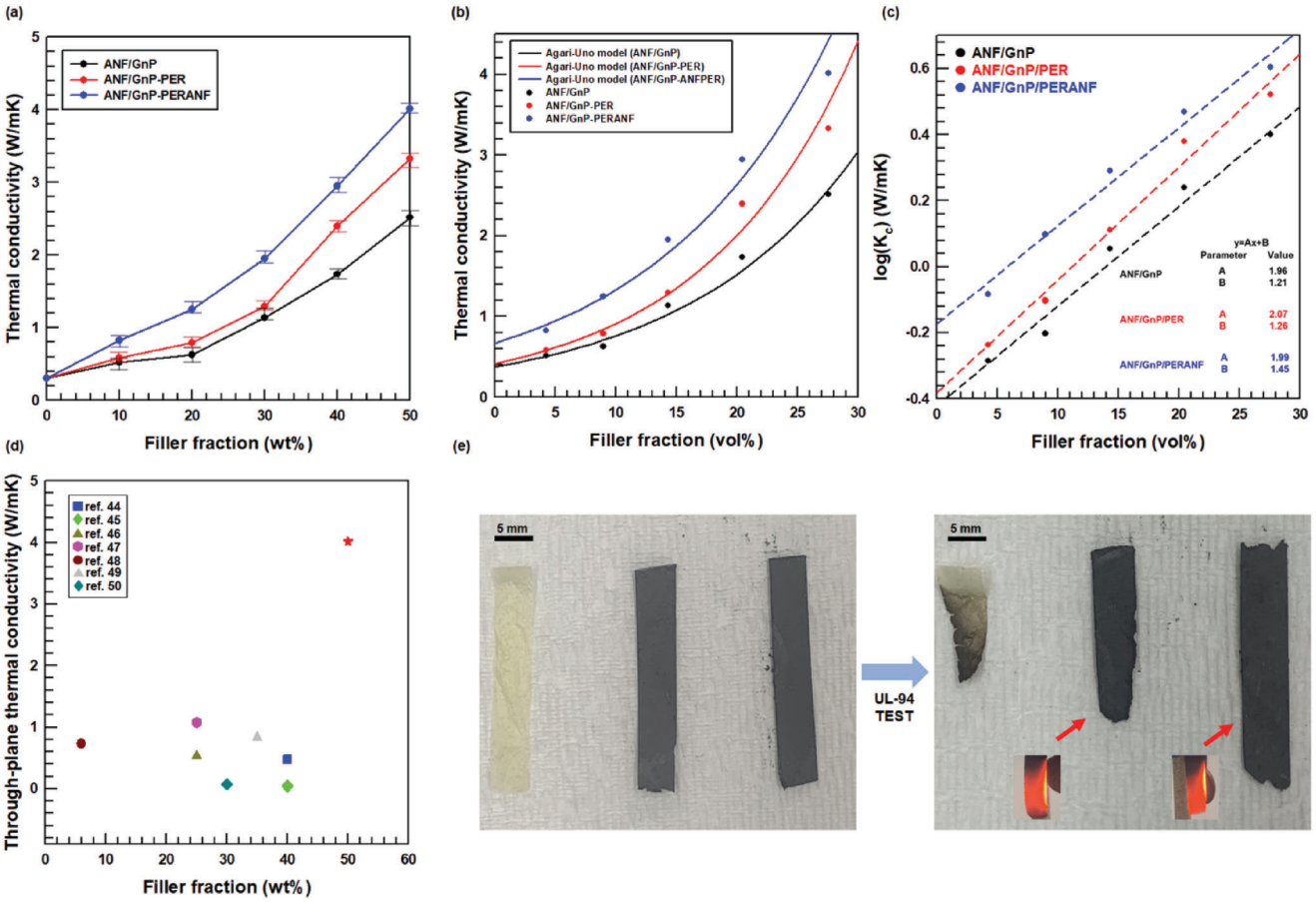


Figure 6. a) Thermal conductivity, b,c) Agari-Uno model, d) Comparison with previous studies,[44,45,46,47,48,49,50] e) UL-94 test of ANF composites.

© 2023 The Authors. Advanced Electronic Materials published by Wiley-VCH GmbH

2199160x, 2023, 12, Downloaded from https://onlinelibrary.wiley.com/doi/10.1002/aelm.202300455 by Chung-Ang University, Wiley Online Library on [26/03/2024]. See the Terms and Conditions (https://onlinelibrary.wiley.com/terms-and-conditions) on Wiley Online Library for rules of use; OA articles are governed by the applicable Creative Commons License

Table 2. Values of C_1 and C_2 for the ANF composites according to the fabrication methods.

	ANF/GnP	ANF/GnP–PER	ANF/GnP–PERANF
Prediction equation of k_c	$k_c = 10^{(3.0164\,Vf\,-\,0.3651)}$	$k_c = 10^{(3.4229\,Vf\,-\,0.3339)}$	$k_c = 10^{(2.9733\,Vf\,-\,0.1371)}$
C_1	1.95	2.15	3.29
C_2	1.27	1.44	1.33

particles, and V_f is the volume of particles such that, $P = (V_f)^{(V_f)^{-2/3}}$ and $V_f = 3c^2 - 2c^3$.[42,43] Here, an alternative model is proposed for the estimation of the thermal conductivity of the two phase-blended composite, which can be determined by the following equation:

$$\log\left(k_p\right) = V_f\ \left[P^* - \log\left(C_1 k_m\right)\right] + \log\left(C_1 k_m\right) \tag{2}$$

where $P^* = X_2\ C_2 \log k_p + X_3 C_3 \log k_3 + \cdots$, C_i is a factor that indicates the formation of thermal conducting paths in the matrix, X_i is the ratio between the fillers in the blended composite, and k_i represents the thermal conductivity of a polymer in a multiphase composite. In our composite system, X_1 is assumed to be 1, and the other coefficients can be neglected. The equation can then be simplified to:

$$\begin{aligned}\log k_c &= V_f\ C_2 \log k_f + \left(1 - V_f\right)\ \log\left(C_1 k_p\right)\\ &= \left(C_2 \log k_p - \log C_1 k_m\right)\ V_f + \log\left(C_1 K_m\right)\end{aligned} \tag{3}$$

We can define C_1 and C_2 by fitting the K_c versus V_f plot based on the experimental data. The calculated slopes ($C_2 \log K_p - \log C_1 k_m$) of the ANF composites are 1.96 (ANF/GnP), 2.07 (ANF/GnP–PER), and 1.99 (ANF/GnP–PERANF). Then, the thermal conductivity of the composites is predicted by substituting the slope and intercept, and the resulting equations are expressed in **Table 2**.

Accordingly, the thermal conductivities (K_c) of the composites can be simplified by the following equation:

$$\log k_c = V_f \times C_2 \times \log k_p + \left(1 - V_f\right) \times \log\left(C_1 \times k_m\right) \tag{4}$$

where C_1 reflects the effect of heat transfer related to the secondary structure of the matrix, and C_2 is a factor that indicates the ease with which a thermal conductive path is constructed by the particles in a composite. According to previous reports, the filler affects the structure of the polymer matrix if C_1 is less than 1. However, in our system, $C_1 > 1$, which suggests the absence of a secondary structure effect. After the PERANF treatment, C_2 significantly increased, which indicates the ease of formation of the heat-transport pathway. As a result, the thermal conductivities of the hot-pressed ANF/GnP–PERANF composites, predicted using the Agari model, are significantly higher than those of the ANF/GnP and ANF/GnP–PER composites, indicating that the fillers form a heat-transport pathway more readily in the presence of an improved filler–filler network.

To validate the exceptional performance of the ANF/GnP–PERANF composites, their thermal conductivity was compared to that reported in recent studies at different filler loadings, as illustrated in Figure 6d. Achieving high thermal conductivity and low filler loading simultaneously poses a significant challenge. However, the ANF/GnP–PERANF composites in our study demonstrated a high through-plane thermal conductivity while maintaining a competitive filler loading. This achievement opens up new possibilities for thermal management applications.

Furthermore, flame retardant tests were conducted to evaluate the flame resistance and thermal stability of the fabricated composites. The UL-94 test was employed to examine the ignition and flame spread of materials on a small scale, assigning flammability ratings such as V-0, V-1, and V-2. A V-0 rating represents the highest level of flame retardancy, indicating no vertical flame spread and no sample dripping. V-1 allows non-flaming drips, while V-2 permits flaming drips.

Table 3 and Figure 6e present the UL-94 ratings of the composites fabricated in our study. The improved flame resistance can be attributed to the formation of a robust and interconnected inorganic filler network within the matrix, facilitated by the GnP particles. This network prevents the passage of oxygen through the compact residue, thereby limiting the availability of combustible materials for thermal degradation or combustion reactions within the composite. Consequently, the enhanced flame resistance of the ANF/GnP–PERANF composites effectively mitigates sudden heat shocks.

To assess the thermal management capabilities of the fabricated composites, they were employed as thermal interface materials (TIMs) on central processing units (CPUs), as depicted in **Figure 7**. Infrared images of the CPUs during operation and the corresponding temperature-heating time graphs are presented in the figure. When the ANF/GnP–PERANF composite was utilized as the TIM, a maximum CPU temperature of 76.14 °C was recorded, while the maximum temperature reached using neat ANF was 88.19 °C. These results indicate that the 3D network composites developed in this study exhibit effective thermal management performance, making them suitable for application as TIMs in electronic devices.

The mechanical properties of the composites were evaluated using a universal testing machine, and the findings are illustrated in **Figure 8**. With the inclusion of raw GnP as a filler, the tensile stress decreased from 128.33 to 84.74 MPa, while the strain reduced from 9.99 to 7.60%. This decrease can be attributed to the

Table 3. UL-94 rating of the composites with different components.

Composites	Drip	UL-94 rating
neat ANF	Yes	NR
ANF/GnP	No	V-1
ANF/GnP–PERANF	No	V-0

© 2023 The Authors. Advanced Electronic Materials published by Wiley-VCH GmbH

2199160x, 2023, 12, Downloaded from https://onlinelibrary.wiley.com/doi/10.1002/aelm.202300455 by Chung-Ang University, Wiley Online Library on [26/03/2024]. See the Terms and Conditions (https://onlinelibrary.wiley.com/terms-and-conditions) on Wiley Online Library for rules of use; OA articles are governed by the applicable Creative Commons License

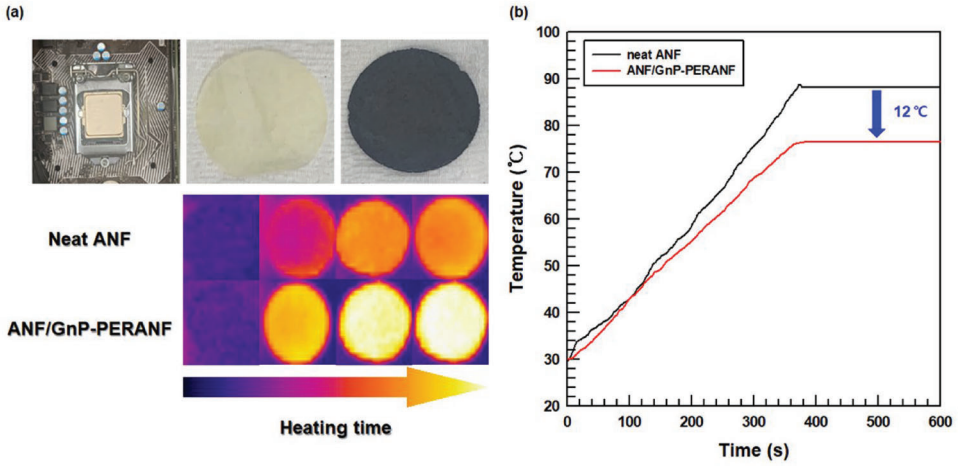


Figure 7. a,b) Heat dissipation performance of ANF/GnP–PERANF composite on CPU.

discontinuous dispersion of GnP, which introduces high defects within the composites. However, in the case of ANF/GnP–PER and ANF/GnP–PERANF composites, there was an improvement in the tensile stress, reaching 147.59 and 163.58 MPa, respectively. Similarly, the strain increased to 8.69% and 11.00%. These enhancements can be attributed to the improved interfacial adhesion resulting from the hydrogen bonding of functional groups among the fillers and the matrix, coupled with the presence of a continuous filler network within the ANF matrix. In summary, the ANF/GnP–PERANF composite demonstrates the potential to serve as an advanced composite in next-generation technology.

3. Conclusions

In order to overcome the limitations of existing polymer composites, such as their low thermal conductivities and inadequate mechanical properties, a novel composite based on ANFs was developed in this study. The primary objective was to enhance the thermal conductivity of the composite. This was achieved by esterification of ANFs and PER onto the surface of GnP, followed by a hot-pressing process. Through this fabrication technique, a 3D filler network was formed, with entangled GnP–PERANF structures embedded within the ANF matrix. The resulting ANF/GnP–PERANF composites exhibited exceptional through-plane thermal conductivity and impressive mechanical properties. These findings highlight the significant potential of ANF-based composites for achieving enhanced thermal conductivity and provide valuable insights for the advancement of thermally conductive polymer composites.

4. Experimental Section

Materials: The acquisition of materials involved Graphene Supermarket (USA) as the supplier of Graphene nano platelets (GnP, ≤ 7 μm). Sigma Aldrich provided the Pentaerythritol (PER) powder, while CNNT Co., Korea was the source for the Aramid nanofiber (ANF). Daejung Chemical Co., Korea supplied the OA dihydrate (with 99.5% purity), nitric acid (with 60% purity), and sulfuric acid (with 98% purity).

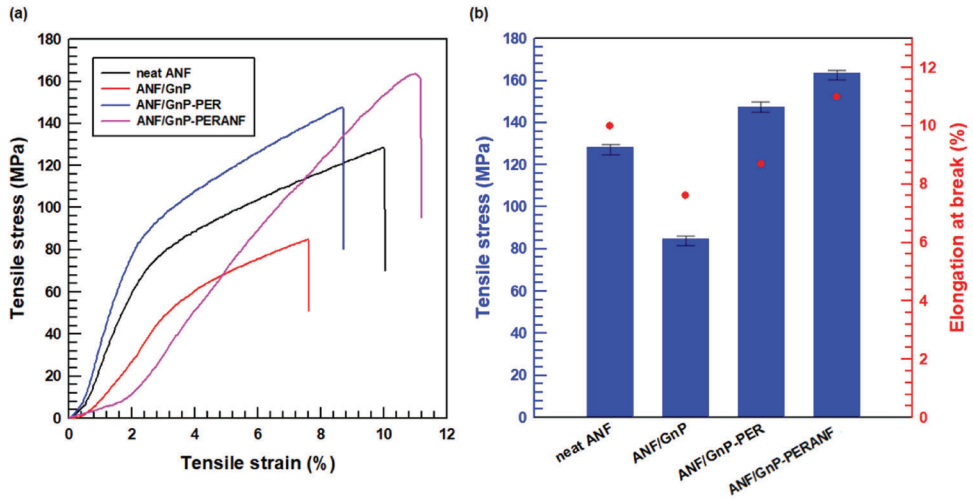


Figure 8. a,b) Mechanical properties of ANF composites.

© 2023 The Authors. Advanced Electronic Materials published by Wiley-VCH GmbH

2199160x, 2023, 12, Downloaded from https://onlinelibrary.wiley.com/doi/10.1002/aelm.202300455 by Chung-Ang University, Wiley Online Library on [26/03/2024]. See the Terms and Conditions (https://onlinelibrary.wiley.com/terms-and-conditions) on Wiley Online Library for rules of use; OA articles are governed by the applicable Creative Commons License

Preparation of GnP–PERANF System: To initiate the oxidation process, 1 g of raw Graphene nano platelets (GnP) was introduced into a 450 mL solution of sulfuric and nitric acid, with a volume ratio of 1:2. The resulting mixture was then subjected to stirring at a temperature of 75 °C for a duration of 6 h. Subsequently, the mixture underwent filtration, followed by multiple water washes and drying at 80 °C.

Moving on to the subsequent step, a composition comprising 1 g GnP–OH, 2 g pentaerythritol (PER), 2 g oxalic acid (OA), and an Aramid nanofiber (ANF) suspension with a weight percentage of 3% was combined with 200 mL of water. The resulting mixture was then subjected to stirring at a temperature of 90 °C for a duration of 5 h to facilitate esterification. Following this process, the mixture underwent filtration, accompanied by water washing to eliminate any unreacted components. Finally, the GnP–PERANF system was dried overnight at 80 °C before it could be utilized further.

Fabrication of Composites: To achieve a uniform mixture, the GnP–PERANF components were dispersed within an ANF suspension with a weight percentage of 3%. Stirring was conducted for a duration of 15 min to ensure homogeneity. Subsequently, the resulting mixture underwent filtration using a vacuum filtration method and was left to dry at ambient temperature for a period of 24 h.

Following the drying process, the ANF film, now in its dried state, was subjected to hot pressing at a temperature of 150 °C and a pressure of 14 MPa. This procedure lasted for 10 min, resulting in the formation of dense ANF/GnP–PERANF composites.

Characterization: The PERANF–GnP surfaces underwent thorough examination using various analytical techniques. Fourier transform infrared spectroscopy (FT-IR) and X-ray photoelectron spectroscopy (XPS) were employed to scrutinize the samples. The FT-IR analysis utilized an advanced Perkin–Elmer Spectrum One instrument in ATR mode, while the XPS measurements were performed using a sophisticated VGMicrotech apparatus. To gain further insights, Raman spectra were acquired utilizing a cutting-edge DXR2xi instrument sourced from Thermo, USA. The Raman measurements involved an argon laser with an excitation wavelength of 514 nm. For a detailed investigation of filler morphology and composite cross-sections, a state-of-the-art Carl Zeiss Sigma instrument was utilized for field-emission scanning electron microscopy (FE–SEM) analysis. Determining the thermal conductivities of the fabricated erythritol composites involved employing the equation $K = \alpha \times \rho \times Cp$. In this equation, K denotes the thermal conductivity measured in W mK^{-1}, α represents the thermal diffusivity in $mm^2\ s^{-1}$, ρ signifies the bulk density in g cm^{-3}, and Cp indicates the heat capacity at room temperature measured in J gK^{-1}. To evaluate the thermal diffusivities of the composites at room temperature, laser flash analysis was performed (10 times per samples; disc-shaped sample; diameter: 12.7 mm). This analysis utilized the NanoFlash LFA 467 instrument, an advanced tool provided by Netzsch Instruments Co. Additionally, the mechanical properties of the composites were rigorously assessed utilizing a reliable universal testing machine (UTM) manufactured by Instron Co. The measurements were conducted with a crosshead speed rate of 2 mm min^{-1}, employing dog-bone-shaped specimens with dimensions of 20 × 4 × 3 mm^3.

Acknowledgements

This work was supported by the Industrial Technology Innovation Program (20019205) funded by the Ministry of Trade, Industry & Energy (MOTIE, Republic of Korea) and also supported by the National Research Foundation of Korea (NRF) grant funded by the Korea government (MSIT) (NRF2022M3H4A1A02076956).

Conflict of Interest

The authors declare no conflict of interest.

Data Availability Statement

The data that support the findings of this study are available from the corresponding author upon reasonable request.

Keywords

polymer-matrix composites (PMCs), surface treatment, thermal conductivity, thermal interface materials (TIMs)

Received: July 10, 2023
Revised: August 24, 2023
Published online: September 22, 2023

[1] L. Xiang, Y. Cheng, X. Yu, Y. Fan, X. Yang, X. Zhang, B. Xie, X. Luo, *Appl. Therm. Eng.* **2023**, *231*, 121005.
[2] A. Ohayon-Lavi, G. Shachar-Michaely, E. Koronio, Y. Keller, E. Yalon, G. Ziskind, O. Regev, *Appl. Therm. Eng.* **2023**, *229*, 120562.
[3] L. He, Z. Gu, Y. Zhang, H. Jing, P. Li, *Energy Fuels* **2023**, *37*, 4835.
[4] J. Li, Z. Ye, P. Mo, Y. Pang, E. Gao, C. Zhang, G. Du, R. Sun, X. Zeng, *Compos. Sci. Technol.* **2023**, *234*, 109948.
[5] L. Zhang, X. Zhang, W. Hua, L. Gao, W. Xie, W. Zhang, *J. Energy Storage* **2023**, *61*, 106819.
[6] F. Yang, Y. Song, Y. Li, J. Li, *Ceram. Inter.* **2023**, *49*, 23844.
[7] G. Yang, L. Zhou, X. Zhang, D. Pan, M. Wang, S. Luo, F. Su, Y. Ji, C. Liu, *Compos. Commun.* **2023**, *37*, 101450.
[8] Z. Wang, D. Hou, F. Wang, J. Zhou, N. Cai, J. Guo, *ACS Appl. Mater. Interfaces* **2023**, *15*, 28626.
[9] M. Li, Y. Sun, D. Feng, K. Ruan, X. Liu, J. Gu, *Nano Res.* **2023**, *16*, 7820.
[10] Y. Zhang, K. Ruan, K. Zhou, J. Gu, *Adv. Mater.* **2023**, *35*, 2211642.
[11] J. Guo, Z. Peng, H. Wang, L. Yang, L. Zhang, C. Li, *Ind. Eng. Chem. Res.* **2023**, *62*, 5877.
[12] X. Wang, W. Cao, Z. Su, K. Zhao, B. Dai, G. Gao, J. Zhao, K. Zhao, Z. Wang, T. Sun, J. Han, J. Zhu, *ACS Appl. Mater. Interfaces* **2023**, *15*, 27130.
[13] R. Lian, Y. Jiang, H. Guan, J. Cui, Q. Gao, L. Liu, X. Chen, C. Jiao, *Polym. Degrad. Stab.* **2023**, *215*, 110444.
[14] T. Yao, C. Zhang, K. Chen, T. Niu, J. Wang, Y. Yang, *Compos. Sci. Technol.* **2023**, *234*, 109934.
[15] A. Bashir, M. Maqbool, A. Usman, R. Lv, H. Niu, L. Kang, Z. Ashraf, S. Bai, *Compos. A. Appl. Sci. Manuf.* **2023**, *173*, 107676.
[16] Z. Zhang, H. Wu, S. Zhang, Y. Wang, Y. Zhang, C. Liu, D. Zhang, B. Jia, D. Guo, A. Chu, X. Qu, M. Qin, *J. Eur. Ceram.* **2023**, *43*, 313.
[17] K. M. F. Shahil, A. A. Balandin, *Nano Lett.* **2012**, *12*, 861.
[18] A. Li, J. Wang, W. He, Z. Wei, X. Wang, Q. He, *Diam. Relat. Mater.* **2023**, *134*, 109790.
[19] Y. Han, K. Ruan, J. Gu, *Angew. Chem. Int. Ed. Engl.* **2023**, *62*, 202216093.
[20] Y. Han, K. Ruan, J. Gu, *Nano Res.* **2022**, *15*, 4747.
[21] H. Li, W. Yang, N. Wu, L. Sun, P. Shen, X. Wang, Y. Li, *Appl. Surf. Sci.* **2023**, *617*, 156485.
[22] Z. Wu, J. Dong, C. Teng, X. Li, X. Zhao, X. Qin, C. Ji, Q. Zhang, *Compos. Commun.* **2023**, *39*, 101543.
[23] F. Kargar, Z. Barani, M. Balinskiy, A. S. Magana, J. S. Lewis, A. A. Balandin, *Adv. Electron. Mater.* **2018**, *5*, 1800558.
[24] Z. Barani, F. Kargar, A. Mohammadzadeh, S. Naghibi, C. Lo, B. Rivera, A. A. Balandin, *Adv. Electron. Mater.* **2020**, *6*, 2000520.
[25] Z. Barani, A. Mohammadzadeh, A. Geremew, C. Y. Huang, D. Coleman, L. Mangolini, F. Kargar, A. A. Balandin, *Adv. Funct. Mater.* **2019**, *30*, 1904008.
[26] J. Renteria, S. Legedza, R. Salgado, M. P. Balandin, S. Ramirez, M. Saadah, F. Kargar, A. A. Balandin, *Mater. Des.* **2015**, *88*, 214.

© 2023 The Authors. Advanced Electronic Materials published by Wiley-VCH GmbH

2199160x, 2023, 12, Downloaded from https://onlinelibrary.wiley.com/doi/10.1002/aelm.202300455 by Chung-Ang University, Wiley Online Library on [26/03/2024]. See the Terms and Conditions (https://onlinelibrary.wiley.com/terms-and-conditions) on Wiley Online Library for rules of use; OA articles are governed by the applicable Creative Commons License

[27] S. Sudhindra, F. Rashvand, D. Wright, Z. Barani, A. D. Drozdov, S. Baraghani, C. Backes, F. Kargar, A. A. Balandin, *ACS Appl. Mater. Interfaces* **2021**, *13*, 53073.
[28] K. Ruan, J. Gu, *Macromolecules* **2022**, *55*, 4134.
[29] A. Subrati, P. Florczak, B. Gurzeda, E. Coy, J. Jenczyk, M. Koscinski, B. Peplinska, S. Jurga, P. Krawczyk, *Carbon* **2021**, *176*, 327.
[30] Y. Yang, M. Wang, Z. Shi, R. Xiao, X. Sun, Y. Chen, *J. Alloys. Compd.* **2021**, *868*, 159128.
[31] W. Lee, J. Kim, *Compos. Sci. Technol.* **2020**, *200*, 108424.
[32] J. Henschen, D. Li, M. Ek, *Carbohydr. Polym.* **2019**, *213*, 208.
[33] W. Jia, Y. Liu, *Cellulose* **2019**, *26*, 8351.
[34] S. Liu, Q. Zhang, S. Gou, L. Zhang, Z. Wang, *Carbohydr. Polym.* **2021**, *251*, 117018.
[35] Y. Liu, Y. Yang, *Renewable Energy* **2018**, *115*, 734.
[36] F. Nazeer, Z. Ma, L. Gao, F. Wang, M. A. Khan, A. Malik, *Compos. B, Eng.* **2019**, *163*, 77.
[37] P. Krawczyk, *Chem. Eng. J.* **2011**, *172*, 1096.
[38] J. M. Lownsbury, J. C. Sharp, E. J. Mann, C. T. Campbell, *J. Phys. Chem. C* **2015**, *119*, 18444.
[39] M. Hu, H. Zhou, X. Gan, L. Yang, Z.-H. Huang, D. W. Wang, F. Kang, R. Lv, *J. Mater. Chem. A* **2018**, *6*, 1582.
[40] T. Xu, Q. Meng, T. Shen, B. Cao, *RSC Adv.* **2015**, *5*, 73737.
[41] M. Bosilj, M. Bozoglu, J. Schmidt, P. M. Aguiar, A. Fischer, R. J. White, *Catal. Sci. Technol.* **2020**, *10*, 776.
[42] Y. Agari, T. Uno, *J. Appl. Polym. Sci.* **1985**, *30*, 2225.
[43] Y. Agari, M. Tanaka, S. Nagai, T. Uno, *J. Appl. Polym. Sci.* **1987**, *34*, 1429.
[44] Q. Li, Z. Xue, J. Zhao, C. Ao, X. Jia, T. Xia, Q. Wang, X. Deng, W. Zhang, C. Lu, *Chem. Eng. J.* **2020**, *383*, 123101.
[45] N. Song, D. Jiao, S. Cui, X. Hou, P. Ding, L. Shi, *ACS Appl. Mater. Interfaces* **2017**, *9*, 2924.
[46] G. Li, X. Tian, X. Xu, C. Zhou, J. Wu, Q. Li, L. Zhang, F. Yang, Y. Li, *Compos. Sci. Technol.* **2017**, *138*, 179.
[47] Z. Hu, S. Wang, G. Chen, Q. Zhang, K. Wu, J. Shi, L. Liang, M. Lu, *Compos. Sci. Technol.* **2018**, *168*, 287.
[48] N. Song, X. Hou, L. Chen, S. Cui, L. Shi, P. Ding, *ACS Appl. Mater. Interfaces* **2017**, *9*, 17914.
[49] X. Wang, P. Wu, *ACS Appl. Mater. Interfaces* **2018**, *10*, 34311.
[50] N. Song, D. Jiao, P. Ding, S. Cui, S. Tang, L. Shi, *J. Mater. Chem. C* **2016**, *4*, 305.

© 2023 The Authors. Advanced Electronic Materials published by Wiley-VCH GmbH

2199160x, 2023, 12, Downloaded from https://onlinelibrary.wiley.com/doi/10.1002/aelm.202300455 by Chung-Ang University, Wiley Online Library on [26/03/2024]. See the Terms and Conditions (https://onlinelibrary.wiley.com/terms-and-conditions) on Wiley Online Library for rules of use; OA articles are governed by the applicable Creative Commons License